AIAA JOURNAL
Vol. 44, No. 4, April 2006

Characterization of Surface Plasma-Induced Wall Flows Through Velocity and Temperature Measurements

Timothy N. Jukes* and Kwing-So Choi†
University of Nottingham, Nottingham, England NG7 2RD, United Kingdom
and
Graham A. Johnson‡ and Simon J. Scott§
BAE Systems, Bristol, England BS34 7QW, United Kingdom

An investigation into the induced airflow around weakly ionized surface glow discharge plasma has been performed in initially static air to study radio-frequency plasma actuators designed for the use of boundary-layer control. Hot-wire and cold-wire anemometry have been used to study the velocity and temperature distribution around a symmetric and an asymmetric electrode configuration. The plasma appears to couple momentum into the ambient air such that it drives a laminar wall jet away from the electrode centerline. Temperature measurements indicate an air temperature rise of 2°C at 1 mm from the plasma, and the flow does not appear to be buoyancy driven. A maximum velocity of 2.5 m/s was observed, indicating the induced flow will be strong enough for flow control applications in low-speed test facilities.

Nomenclature

E	=	applied voltage, V
I	=	current, A
P	=	power, W
Re_δ	=	Reynolds number of wall jet, $U_{\max}\delta_{1/2}/\nu$
T	=	temperature, °C
t	=	time, s
t_{AC}	=	repetition period, 2/PRF (pulse repetition frequency), s
t^*	=	nondimensional time, $tU_{\max}/\delta_{1/2}$
U	=	velocity, m/s
$U_{\max}$	=	maximum velocity, m/s
U^*	=	nondimensional velocity, $U/U_{\max}$
u_τ	=	friction velocity, m/s
x	=	streamwise distance, normal to electrode centerline, m
y	=	wall-normal distance, m
y^*	=	nondimensional wall-normal distance, $y/\delta_{1/2}$
y^+	=	nondimensional wall-normal distance, yu_τ/ν
z	=	direction parallel to electrode centerline, m
$\delta_{1/2}$	=	jet half-width, m
ν	=	kinematic viscosity, m^2/s

I. Introduction

RADIO-FREQUENCY (rf) glow discharges have been used in microelectronic device fabrication, ozone generation, and in gas laser excitation for some time.[1,2] Such discharges, operating at atmospheric pressure, have recently become a topic for flow control applications because of the plasma exerting a body force on the ambient fluid and thus creating a flow. Typical excitation is at several kilohertz and several kilovolts.

Such devices have been shown to produce flow velocities of the order of 1 m/s in initially static air.[3,4] Though this induced flow is small, it is postulated that it can be used for flow control by manipulating low-speed regions (e.g., the viscous sublayer of a turbulent boundary layer) to produce global gains such as skin-friction drag reduction and separation control. There are many potential advantages over conventional flow-control methods. The plasma actuator is a simple device with no moving parts and eliminates the need for complicated ducting, as is the case for many other actuators. Also the plasma process is fast acting and can be of low power and can therefore have a realistic possibility of scaling to flight conditions.

Johnson and Scott[4] and Scott et al.[5,6] have previously demonstrated that such surface discharges, based on corona-plasma technology, can induce small, but significant, effects in subsonic airflow. The plasma was used as an efficient boundary-layer trip and to control the leading-edge vortices on swept and delta wings. This technology proved very reliable with an extremely reproducible performance at atmospheric pressure and, being relatively exempt from erosion, offered running times of at least several hours.

The plasma has been observed to exert a paraelectric electrohydrodynamic body force that will drive the ambient air away from the plasma[7–9] and has been modeled using the Lorentz equation.[10,11] Plasma actuators have been used to alter the lift and drag on airfoils,[10,12,13] turbine blades,[10,14,15] to alter the boundary layer over flat plates,[9] and to affect the vortex shedding from circular cylinders.[16] Attempts have been made to numerically simulate the plasma-induced airflow by using an electrohydrodynamic body force term in the Navier–Stokes equations.[17] It is thought the induced flow is caused by Lorentzian collisions between ions accelerated in the steep electric field gradients within the plasma and the neutral gas particles.[2,3,7]

The aim of this investigation is to characterize the velocity and temperature of the induced airflow over surface plasma actuators in initially static air so that strategies can be formulated for using the device in flow-control applications. The effect of plasma actuator geometry has been studied be Enloe et al.,[18,19] and actuators are commonly asymmetric such that forcing is produced in one direction only. Two actuator configurations are studied here. First, a symmetric actuator is used, which produces bidirectional forcing. This is a more generic actuator because it is immune to the geometry of the lower electrode.[18,19] In addition, an asymmetric actuator that produces unidirectional forcing is studied. Our main interest is in using the device for drag reduction by simulating a mechanical

Presented as Paper 2004-2216 at the AIAA 2nd Flow Control Conference, Portland, OR, 28 June–1 July 2004; received 24 April 2005; revision received 21 August 2005; accepted for publication 19 October 2005.

*Research Postgraduate, School of Mechanical, Materials and Manufacturing Engineering, University Park. International Student Member AIAA.
†Professor of Fluid Mechanics, School of Mechanical, Materials and Manufacturing Engineering, University Park. Senior Member AIAA.
‡Principal Scientist, P.O. Box 5, Advanced Technology Center, Mathematical Modeling Department, Filton.
§Senior Principal Scientist, P.O. Box 5, Advanced Technology Center, Optics and Laser Technology Department, Filton.

spanwise oscillation movement in a turbulent boundary layer. Previous studies have shown this is an effective method for viscous drag reduction, yielding reductions of up to 45% (Ref. 20). This paper describes the plasma generation system used for the investigation and discusses some measurements of the plasma-air interaction.

II. Experimental Arrangement

A. Plasma Generation System

There are two main components to our surface plasma generation system for boundary-layer control: the electrode sheet and the power supply. The electrode layout consists of a pair of electrodes, one patterned and one usually continuous, separated by a dielectric layer (Fig. 1), across which a pulsed voltage is applied. Weakly ionized plasma is formed around the electrode edge, occurring as a light purple glow extending for around 2 mm. This dielectric barrier discharge (DBD) can be operated under a wide range of pressures from vacuum to atmospheric. The plasma is initiated by locally ionizing the gas around the exposed electrode, and a surface discharge subsequently spreads out, driven by the electrical circuit and capacitively coupled to the rear, continuous electrode. Our electrode sheets are made from Mylar, with a typical thickness in the 125–250-μm range, double sided with copper. One or both sides can be etched. The plastic sheets are molded and attached to two-dimensional surfaces with double-sided adhesive tape or adhesive spray. Our largest electrode system to date[4] consists of two 80×30 cm long sheets positioned around the leading edge of a wing. In this study, the plasma-induced airflow around a single symmetric and a single asymmetric electrode has been studied in initially static air at atmospheric pressure. The symmetric electrode was a photochemically etched 90-mm-long, 200-μm-wide, and 17-μm-thick copper electrode with 17-μm-thick solid copper backing. This produces equal plasma formation on both sides of the exposed electrode. The asymmetric electrode was an 85-mm-long, 1-mm-wide, 17-μm-thick upper electrode with a lower electrode 9 mm wide, flush with the edge of the exposed electrode. Here, plasma is formed only on the side of the electrode under which the lower electrode is placed. In both cases the dielectric was 250-μm-thick Mylar sheet (dielectric constant = 3.1 at 1 MHz). The plasma electrode sheets are attached to a metal heat sink and flush mounted to the underside of a flat test plate within a closed-return wind tunnel with octagonal working section, 508 mm high and 508 mm wide. Connections to the electrode sheet are made via short coaxial cables. All measurements have been taken with the wind tunnel turned off.

The plasma power supply is based on a semiconductor switched, bipolar output circuit, running at ± 300 V and discharging into a pulse transformer with a resistively ballasted output. The power supply contains internal voltage probes, and the current supplied to the electrode sheet is monitored using a current shunt. Two pulse generators control the supply. The output is in the form of alternating polarity pulses, $\sim$4 kV amplitude, with variable charge time of typically a few microseconds (set to match the charging time

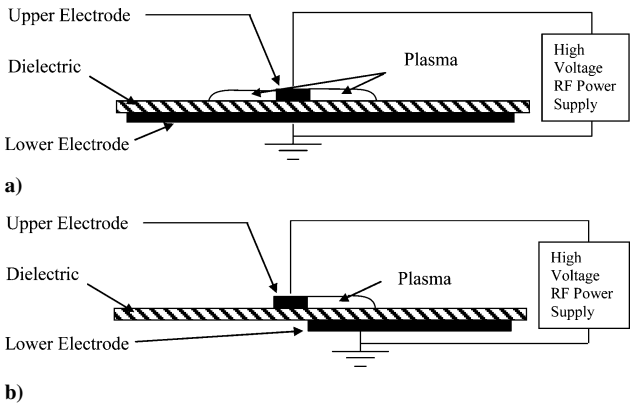

Fig. 1 Plasma electrode sheet cross-section schematic: a) symmetric electrode configuration and b) asymmetric electrode configuration. Not shown to scale.

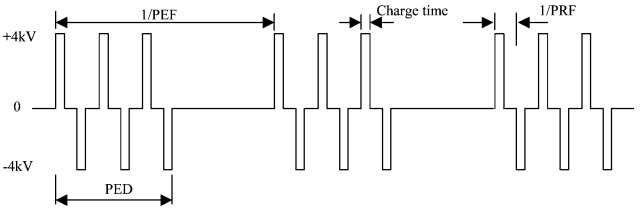

Fig. 2 Plasma excitation parameters schematic.

of the coaxial lead and electrode sheet), variable pulse repetition frequency (PRF), pulse envelope duration (PED), and pulse envelope frequency (PEF). Figure 2 explains these excitation parameters. Note that the pulses driving the plasma are created by a rectangular waveform from a signal generator. These are positive pulses ($\sim$10 V) at the pulse repetition frequency, although these are then converted into alternating negative and positive high voltage pulses within the power supply. The current test sheets have been used, problem free, for a total time of over 50 h.

B. Velocity and Temperature Measurements

A Dantec 55P16, 5-μm-diam, hot-wire probe with a Dantec 56C series anemometry system was used to study the velocity distribution around the electrode. Data were collected by an IoTech 488/8s ADC and stored on a PC. The wire was oriented parallel with the electrode (normal to the induced flow) and used in constant-temperature mode at an overheat ratio of 1.8. Low-speed calibration of the wire was performed in the settling chamber of the wind tunnel at 0.1–2.5 m/s, where a fourth-order polynomial fit was used. The following coordinate system is adopted: x is the lateral direction from the electrode centerline parallel to the wall, y is the wall-normal direction, and z is the direction along the electrode length. The probe was traversed around the electrode at 2-mm intervals away from the electrode centerline (-12 mm $\leq x \leq$ 12 mm, where $x = 0$ is the electrode centerline) and at 0.25-mm intervals in the wall-normal direction (0.25 mm $\leq y \leq$ 4 mm, where $y = 0$ is the electrode surface). The position was controlled using a three-axis traverse mechanism with positional resolution less than 2.5 μm. Probe positioning relative to the electrode was achieved using a charge-coupled-device camera with a zoom lens, giving positional accuracy better than 50 μm.

For temperature measurements, a Dantec 55P31, 1-μm-diam, 0.4-mm-long platinum wire probe was used in constant-current mode. This type of probe is relatively insensitive to flow, and data collection was extended to a wall-normal distance of 11 mm. This is a resistive device, with temperature linearly proportional to output voltage and a frequency response of 2.3 kHz. Temperature sensitivity of the cold wire was obtained from the measured sensor and cable resistance, taking the effect of ambient temperature drift into account over the course of the experiment.

III. Results

A. Plasma Characteristics

Typical voltage and current waveforms during a single plasma cycle are shown in Fig. 3. Note that the current shown is that delivered to the plasma sheet and contains the current flowing in the plasma and that charging the capacitance of the dielectric.[21] Gibalov and Pietsch[22] have performed a detailed study of the surface discharge development, and Enloe et al.[19] present details of the self-limiting nature of a DBD. Plasma is formed when the upper (exposed) electrode is at high enough negative potential relative to the dielectric surface for electrons to be emitted. These subsequently ionize the surrounding air and build up charge on the dielectric. A secondary discharge is initiated at the end of the pulse without simultaneously consuming energy from the electrical circuit.[21] In Fig. 3, discharge is initiated once the potential exceeds 2 kV and continues until the applied voltage has reached the maximum value (4.1 kV on positive pulses, -3.7 kV on negative pulses). At the maximum, the applied voltage ceases to increase, and the surface charge buildup will oppose the electrode potential. This inhibits further electron emission, and the plasma quenches. Once the applied voltage is

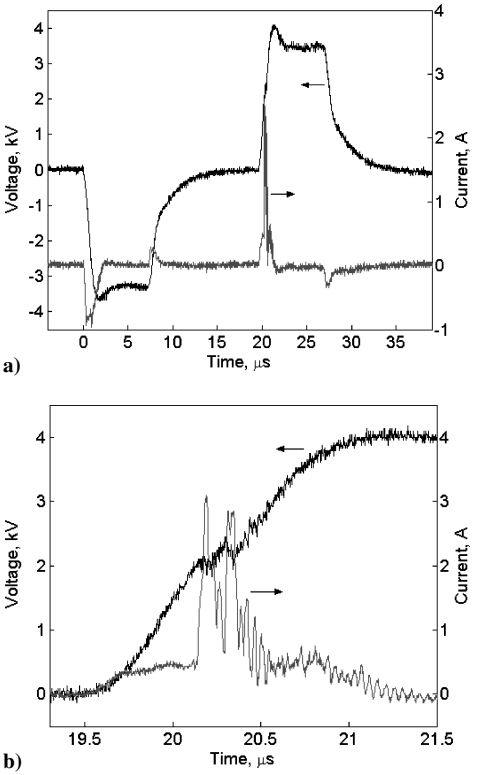

Fig. 3 Voltage and current waveforms: a) during a full ac cycle and b) detail of positive pulse. PRF = 50 kHz, charge time = 7 μs, and E_{max} = 4.1 kV.

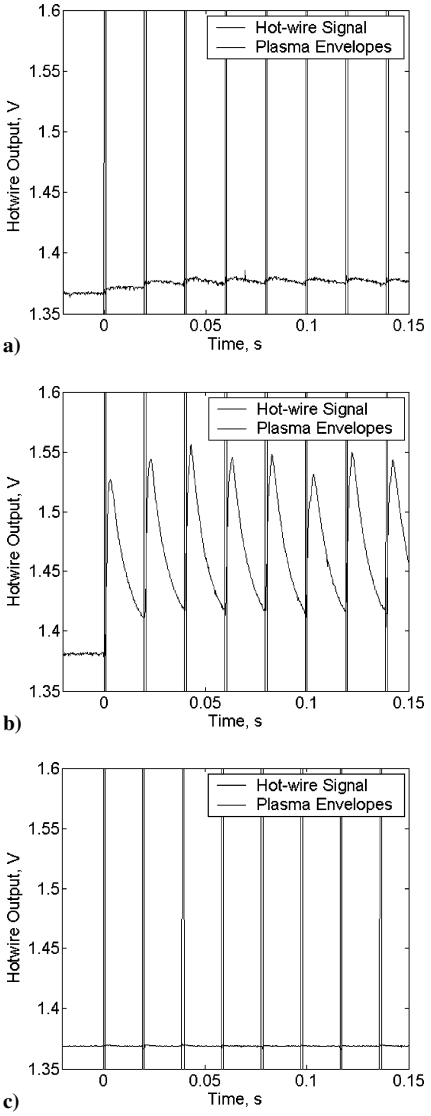

Fig. 4 Hot-wire signals around the symmetric electrode: a) $x = 0$ mm, $y = 4$ mm, $r = 4$ mm; b) $x = 4$ mm, $y = 0.5$ mm, $r = 4.03$ mm; and c) $x = 4$ mm, $y = 0.5$ mm, $r = 4.03$ mm with 250-μm-thick Mylar placed between the electrode and probe. Plasma envelopes of 1 ms duration occur at a frequency of 50 Hz (i.e, every 20 ms). PRF = 50 kHz, charge time = 7 μs, and E_{max} = 4.1 kV.

turned off, there is a momentary reverse flow of current caused by the resulting electric field of the surface charge. This process also applies to positive-going pulses, except that the charge available is limited to that deposited on the dielectric on the previous half-cycle. The positive-going waveforms have a more irregular current pulse, consistent with the behavior of a DBD[19] (Fig. 3b). On integrating voltage and current waveforms it is found that 1.1 mJ (25 μJ/cm) are deposited into the plasma for positive pulses and 1.6 mJ (30 μJ/cm) for the negative pulses. Measurements in initially static air showed that it was the negative-going waveforms that produced the greater force.[19] It is thought that collisions between the ions and background gas are the mechanism for coupling momentum into the airflow.[2]

B. Preliminary Hot-Wire Study

There are many issues relating to the use of the hot-wire probe for measuring the airflow around a high-voltage electrical source, such as plasma. First, the formation of plasma can cause electrical interference in the anemometry system. Despite efforts to reduce the electrical noise by signal filtering and shielding, the anemometer signal during a plasma pulse could include interference. The presented results are based only on data taken after each plasma envelope and are therefore devoid of this electromagnetic (EM) noise. Figure 4 shows the hot-wire voltage signal at nearly identical radial distances vertically above (Fig. 4a) and to the side (Fig. 4b) of the electrode. The hot-wire signals are markedly different, suggesting they are attributed to a flow phenomenon, not electrical noise. In addition, the hot wire has been placed at the side of the electrode with a small piece of Mylar between the plasma and probe in order to block the induced flow. The probe signal is shown in Fig. 4c. The hot-wire voltage change is small (<3 mV), confirming the signal of Fig. 4b is from an induced flow.

Experiments with (broken) hot-wire probes show that flashover will occur between the high-voltage electrodes and the anemometer at a radial distance of ~3 mm. In one instance, a working probe was traversed within 3 mm of the electrode and arcing occurred, vaporizing the sensor wire and part of the prongs. Damage was caused to the anemometry system. Hence, no data can be taken in a region less than 3 mm around the electrode. This is approximately 20 viscous units of the boundary layer in the current experimental facility.

Preliminary results show that there is some effect on the hot-wire measurements because of the presence of the wall. An apparent velocity is observed in still air at wall-normal distances less than 1.25 mm (250 wire diameters) because of the wall drawing heat from the hot wire and the anemometer compensating by increasing the wire temperature/voltage. Other studies show the wall effect generally occurs at distances less than 50 wire diameters[23] and for $y^+ < 3$ in a turbulent boundary layer.[24] Although the wall effect error will decrease when airflow is present, the results presented should be treated with some caution, particularly for the data close to the wall.

The hot wire will also respond to the rise in ambient air temperature as a result of the plasma heating the flow. An overheat ratio of 1.8 has been used to minimize the probes sensitivity to temperature changes. The wall effect would tend to cause the measured velocity to be higher than the true velocity, whereas an increase in ambient fluid temperature will tend to cause the measured velocity to be lower.

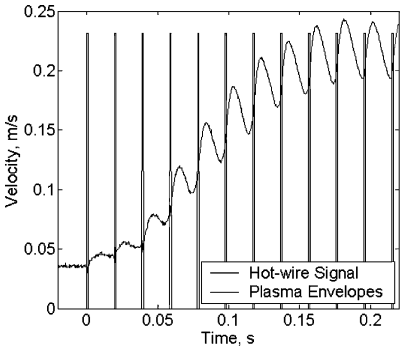

Fig. 5 Hot-wire signal at $y = 1$ mm, $x = 8$ mm: PRF = 50 kHz, charge time = 7 μs, E_{max} = 4.1 kV, PED = 1 ms, and PEF = 50 Hz. Symmetric electrode sheet.

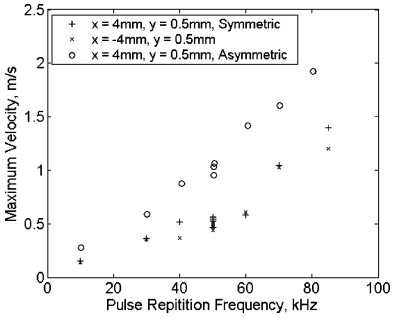

Fig. 6 Variation of maximum phase-averaged velocity with PRF at $x = \pm 4$ mm, $y = 0.5$ mm: charge time = 7 μs, E_{max} = 4.1 kV, PED = 1 ms, and PEF = 50 Hz.

C. Parametric Testing

The hot-wire velocity data yield information on two timescales. There is an effect of the plasma on the flowfield after each individual plasma pulse and a cumulative effect of each subsequent plasma pulse. The phase-averaged velocity profile after a plasma pulse is obtained by ensemble averaging the hot-wire signal between pulses after the flowfield is established. Figure 5 shows a typical hot-wire signal at $y = 1$ mm, $x = 8$ mm. It can be seen that some time is necessary before the airflow exhibits similar behavior between each subsequent plasma envelope ($\sim$0.4 s or 20 pulses within the entire measurement area, although this is shorter at closer distances to the electrode). The quasi-steady fluctuation in velocity is then repeated each cycle until the end of the total plasma on period ($t = 1.3$ s).

A parametric study was undertaken on the effects of the PRF, PEF, and PED on the flowfield. All parameters were varied independently from a base case of PRF = 50 kHz, charge time = 7 μs, $E_{max} = 4.1$ kV, PED = 1 ms, and PEF = 50 Hz. The power supply is limited to a PRF of 90 kHz and a duty cycle of 50% [=PED(s) $\cdot$ PEF(Hz)], though the duty cycle was not increased above 25% for fear of thermal failure of the electrode sheet.

The maximum phase-averaged velocity is shown as a function of PRF, PEF, and PED in Figs. 6–8, respectively. This is defined as the maximum phase-averaged velocity observed between plasma envelopes at $x = \pm 4$ mm, $y = 0.5$ mm. It is found that for all tests this is the location of the peak velocity for which there are data. The differences in the peak velocity observed on either side of the electrode for the symmetric case in Figs. 6–8 might have resulted from probe positional error and asymmetry in the formation of plasma caused by surface irregularities.

The induced airflow is observed to vary slightly nonlinearly with the PRF for both the symmetric and asymmetric electrode sheets. For the symmetric electrode sheet a maximum of 1.4 m/s was observed at a PRF of 85 kHz. This is a 280% increase of the velocity induced with a PRF of 50 kHz. For the asymmetric case, the induced velocity is nearly 90% higher than for the symmetric case, with a maximum flow of 1.95 m/s being observed at a PRF of 80 kHz. Below excitation frequencies of 3 kHz for both cases, no plasma could be detected, and the hot-wire signals were too small to distinguish from background noise.

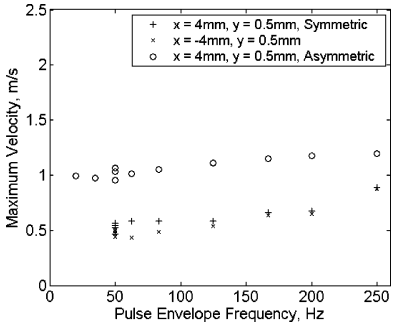

Fig. 7 Variation of maximum phase-averaged velocity with PEF at $x = \pm 4$ mm, y = 0.5 mm: PRF = 50 kHz, charge time = 7 μs, E_{max} = 4.1 kV, and PED = 1 ms.

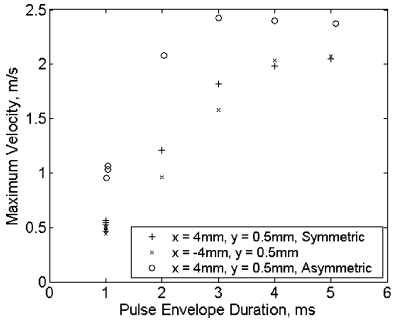

Fig. 8 Variation of maximum phase-averaged velocity with PED at $x = \pm 4$ mm, $y = 0.5$ mm: PRF = 50 kHz, charge time = 7 μs, E_{max} = 4.1 kV, and PEF = 50 Hz.

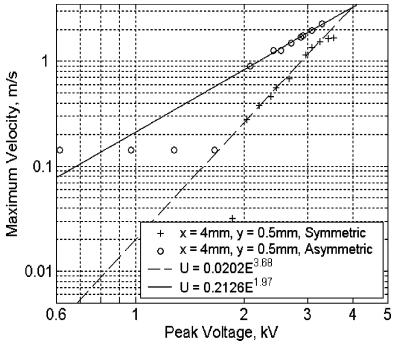

Fig. 9 Variation of maximum phase-averaged velocity with applied voltage at $x = 4$ mm, $y = 0.5$ mm: PRF = 60 kHz, charge time = 7 μs, PEF = 100 Hz, and PED = 2 ms.

A small linear increase in the velocity was achieved by increasing the PEF (i.e., reducing the time between envelopes). For the symmetric case, a maximum velocity of 0.9 m/s was obtained at a pulse envelope frequency of 250 Hz (25% duty cycle). This is a 180% increase to the velocity generated with a pulse envelope frequency of 50 Hz (5% duty cycle). For the asymmetric case, a maximum of 1.2 m/s was observed, and again the induced airflow velocity is around 90% higher than the symmetric case.

A significant linear increase in induced velocity can be achieved by increasing the PED. A maximum velocity of 2.1 m/s was achieved by increasing the PED to 5 ms (25% duty cycle) with the symmetric sheet, whereas a maximum of 2.4 m/s was obtained with the asymmetric sheet. However, both electrode sheets exhibit a saturation effect for PED > 4 ms, whereby increasing the PED further does not increase the induced airflow, thus indicating the timescale of momentum coupling between the plasma and air.

The variation of maximum phase-averaged velocity with applied voltage is shown in Fig. 9. The hot wire was placed at $x = 4$ mm,

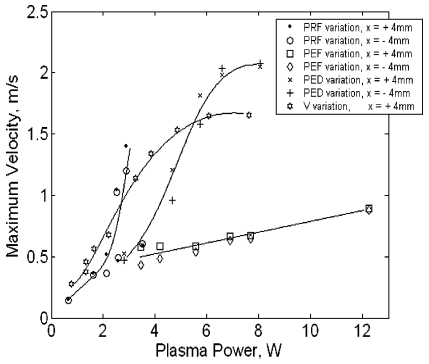

Fig. 10 Variation in phase-averaged maximum velocity with plasma power, through varying individual plasma excitation parameters: symmetric sheet, $y = 0.5$ mm.

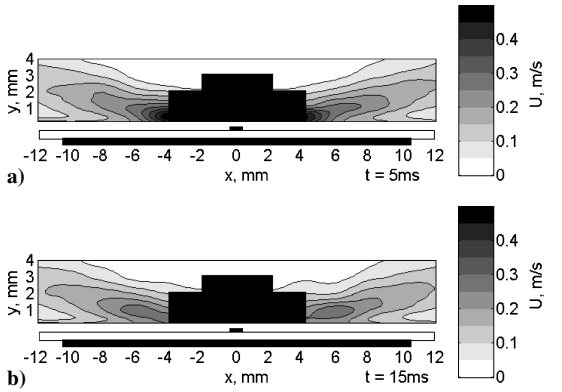

Fig. 11 Phase-averaged velocity contours around a single symmetric electrode. Electrode sheet shown below each plot is not to scale. Blackened area represents where no hot-wire data are taken because of the high risk of flashover: a) $t = 5$ ms and b) $t = 15$ ms.

$y = 0.5$ mm with plasma parameters such that a substantial jet velocity is generated at the maximum applied voltage. It is evident that a minimum voltage of 2 kV is required for plasma to be generated and a flow to be established. Below this voltage, no plasma can be seen with the naked eye, and no spikes were evident in the current waveform. Above this threshold, the generated flow velocity increases rapidly with applied voltage, limited only by the power supply. Previous studies have shown that the plasma-induced flow velocity is proportional to $\frac{7}{2}$ power of voltage[18] ($U_{\max} \propto E^{7/2}$), and our results for the symmetric electrode sheet suggest a similar trend. However, for the asymmetric case the variation in induced velocity appears to vary as E^2.

The power input into the plasma P is calculated as

$$P = \frac{\mathrm{PRF}}{2}\mathrm{PED} \cdot \mathrm{PEF} \int_0^{t_{\mathrm{AC}}} (\mathrm{EI})\, \mathrm{d}t \qquad (1)$$

where t_{AC} is the time to complete one ac cycle (i.e., 2/PRF). The voltage and current waveforms are obtained from averages of multiple cycles to eliminate random noise. The maximum observed velocity is plotted against power in Fig. 10 for the symmetric electrode sheet. Similar results are observed for the asymmetric case. A reasonable collapse of data is observed through variation of the PRF, PED, and $E_{\max}$, suggesting the induced velocity is proportional to the power delivered to the electrode sheet. The power calculated here is not equivalent to the power consumed by the plasma and contains contributions of dielectric heating and electric losses. It appears to be more efficient to increase the jet velocity by increasing the PRF, and it is evident that limited gains can be made by increase of the PEF. The effect of reducing the charge time has also been studied. The induced velocity is not affected by a reduction in this parameter, although the charge time was not reduced below 5 μs. Improvements to the power supply and interconnecting cables can reduce the rise and fall time of the voltage signal, thus enabling higher oscillation frequencies, and hence flow velocities, to be generated.

The fluid power produced by the plasma has been evaluated from the ensemble-averaged velocity distribution at $x = \pm 4$ mm. Fluid power of the order of 10^{-4} W is created by the plasma, and the mechanical efficiency of the device is of the order 10^{-2}%, similar to the results of Enloe et al.[18] This is, however, based on the electrical power dissipated in the whole system, not just the plasma. The actual efficiency of the plasma itself is expected to be significantly greater than this.

D. Velocity Profile

A contour plot of the phase-averaged velocity profile of the symmetric base case at $t = 5$ and 15 ms is shown in Fig. 11 (where $t = 0$ corresponds to the initiation of the 1-ms duration plasma envelope). For these results, the plasma was created with PRF = 50 kHz, charge time = 7 μs, $E_{\max} = 4.1$ kV, and split into envelopes of PED = 1 ms, PEF = 50 Hz. This pulse train was activated for a total of 1.3 s. The position of the electrode is given below each plot, and the blackened area represents the region for which no data were taken because of

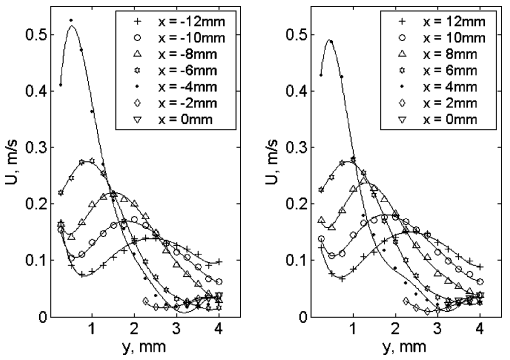

Fig. 12 Velocity profiles on either side of the symmetric electrode. Curves are polynomial fits to the data points: $t = 5$ ms.

the danger of arcing between the electrode and the probe. These data have been spatially and temporally corrected for the cold-wire temperature measurements of Sec. III.E. First, the induced airflow is nearly symmetric around the electrode centerline. This is to be expected from the electrode geometry. A decelerating, broadening velocity profile is observed traveling in either direction away from the plasma. A peak velocity $U_{\max}$ of 0.51 ± 0.05 m/s is observed at the closest lateral location ($x = 4$ mm) and 0.5 mm from the electrode surface. Though this induced velocity is lower than the maximum that occurred during parametric testing (2.1 m/s), the presented results are representative of all of the preceding tests.

The peak velocity is observed within the measurement area, 5 ms after the start of the plasma envelope (Fig. 11a). After this time a steady decrease in velocity is observed throughout the measurement area, though the general characteristics of the profile remain the same (Fig. 11b). The contour plots suggest a velocity that is even higher closer to the electrode. However, measurement limitations as a result of high-voltage flashover inhibit data collection in this region. Figure 12 shows the velocity profiles on either side of the electrode. The plotted curves are polynomial fits to the data points. The nondimensional profiles have been plotted in Fig. 13, normalizing with the maximum velocity across the profile $U_{\max}$ and the jet half-width $\delta_{1/2}$, defined as the distance to the point where the jet velocity has dropped to $U_{\max}/2$. Also plotted are the theoretical profiles of the turbulent and laminar wall jet, studied by Glauert.[25] The plasma-induced airflow appears to be similar to a laminar wall jet, also reported by Roth et al.[26] The Reynolds number of the flow, based on $U_{\max}$ and $\delta_{1/2}$ is $Re_\delta = 40$. Chun and Schwarz[27] show the critical Reynolds number of a laminar wall jet is $Re_{\delta\mathrm{crit}} = 57$. This profile is typical for all times between plasma envelopes. Discrepancies occur in the outer regions of the wall jet ($y^* > 1.2$). These errors occur because of a wall-normal component of velocity in the outer region ($-v$), as a result of the entrainment action of the flow. The profile also deviates from the theoretical laminar wall jet profile

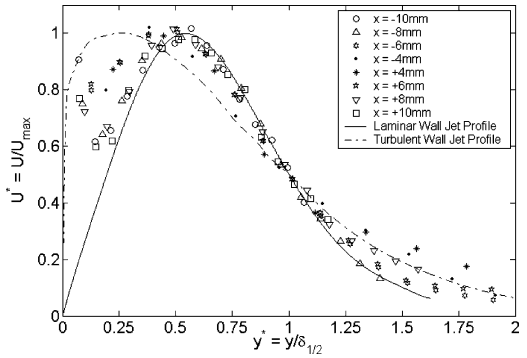

Fig. 13 Nondimensional velocity profile. Normalized with the maximum velocity U_{max} and jet half-width $\delta_{1/2}$. The theoretical profiles of the laminar and turbulent wall jet are plotted from Glauert[25]: $t = 5$ ms.

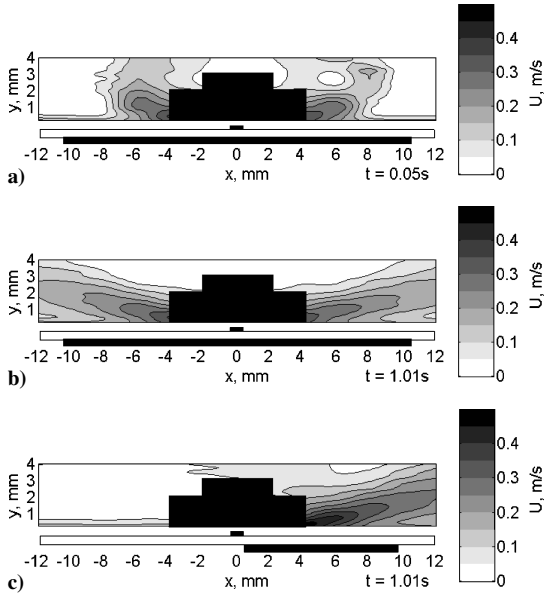

Fig. 14 Pulse-averaged velocity contours around a single electrode. Electrode sheet shown below each plot is not to scale: a) symmetric electrode, $t = 0.05$ s; b) symmetric electrode, $t = 1.01$ s; and c) asymmetric electrode, $t = 1.01$ s.

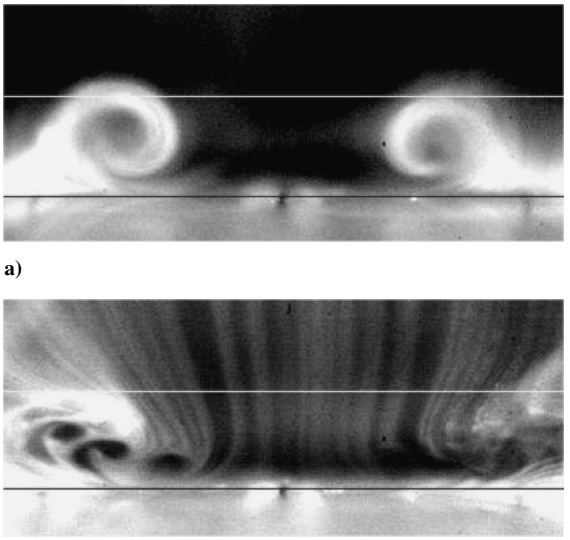

Fig. 15 Smoke wire flow-visualization images around the symmetric plasma electrode. The plasma electrode can be seen in the center of the images, and the smoke wire is located 10 mm below. Note that the images have been rotated 180 deg. Horizontal field of view is 24 mm ($x = \pm 12$ mm). Lines show the location of $y = 0$ and $y = 4$ mm.

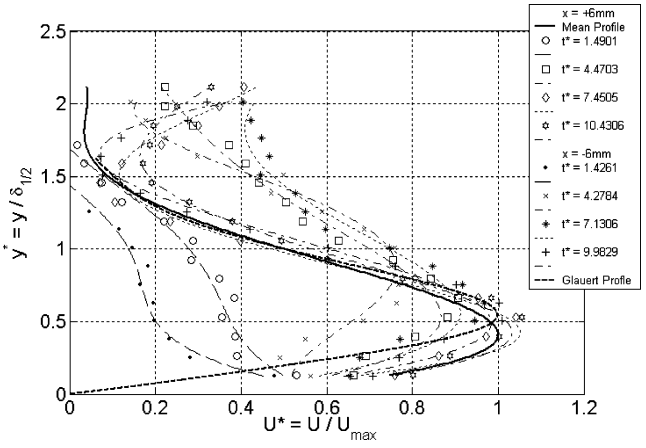

Fig. 16 Development of the wall jet. Pulse-averaged velocity plotted nondimensionally at $x = 6$ mm (open symbols) and $x = -6$ mm (crossed symbols) at various midpulse times.

in the inner region ($y^* < 0.4$). This is a result of the near-wall effect, as discussed in Sec. III.B.

The pulse-averaged velocity profile, taken as the time-averaged velocity between plasma pulses, is shown as a contour plot at $t = 0.05$ and 1.01 s in Fig. 14. The pulse-averaged velocity profile is constant with time after $t = 0.4$ s and takes the form of Fig. 14b. Also plotted in Fig. 14c is a contour plot of the asymmetric electrode configuration at $t = 1.01$ s. The flow characteristics around the asymmetric electrode sheet are similar to the symmetric case, except the flow is clearly unidirectional and the induced flow velocity is higher. The velocity profile and similarity to a laminar wall jet are as above, and we consequently focus on the symmetric case.

Figure 15 shows flow-visualization images of the symmetric electrode using a smoke wire at similar times to Fig. 14. The quasi-steady flow can be seen in Fig. 15b, whereby a series of wall jets are produced in either direction. The individual jets are created during each plasma pulse and agglomerate at some distance downstream. Note that the airflow is primarily in the negative y direction above the electrode and in the $\pm x$ direction for $y < 2.5$ mm. The hot-wire error associated with this nonparallel flow is less than 11% for $y < 2.5$ mm.

The development of the jet profile can be seen in Fig. 16. This shows the nondimensional flow velocity U^* and the wall-normal distance y^* at various times throughout the plasma pulse. Data at 6 mm on either side of the electrode are shown because the data are fine enough to encapsulate the location of the maximum velocity and the velocity magnitude is significant ($U_{max} \approx 0.25$ m/s; see Fig. 12). The final velocity profile, taken as the average velocity profile for $t > 0.8$ s, is identical at both of the streamwise locations, and it is expected that the evolution of the jet is similar to either side of the electrode. The flowfield seems to primarily develop in the outer region, with the velocity overshooting the final profile while the near-wall flow increases in magnitude more slowly. This distortion in the outer jet profile is observed traveling away from the wall with time ($y^* > 0.5$) and has moved past this hot-wire location by $t^* \approx 7$. This motion is related to a pair of vortices created at the electrode at the moment of plasma creation, which can be clearly seen in the flow visualization of Fig. 15 and the temperature profile of Sec III.E. There is no evidence to suggest that the plasma forms differently during each pulse envelope, and consequently it is believed that the momentum imparted into the flow is the same each time. For $t^* > 10$, the pulse-averaged velocity profile becomes time invariant. The induced flow is therefore a quasi-steady pulsed laminar wall jet, with small fluctuation in velocity between pulse envelopes, preceded by a development period in which vortices are created. These initiation vortices are inherent in the plasma flow because of the slip-wall condition within the plasma and the nonslip boundary condition outside.

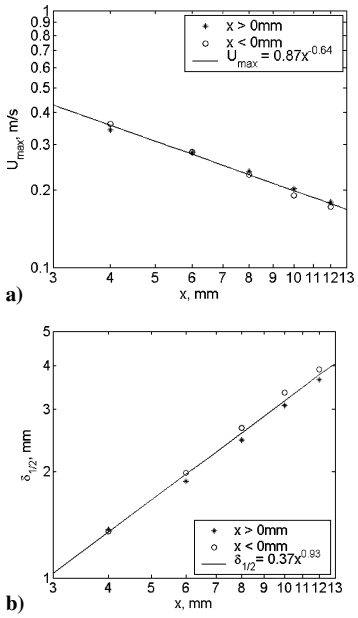

Fig. 17 Variation of steady-state pulse-averaged parameters with distance from electrode centerline: a) variation of maximum velocity and b) variation of jet half-width.

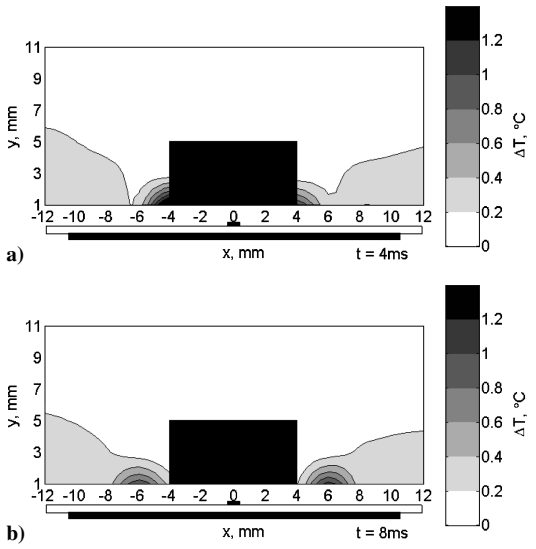

Fig. 18 Phase-averaged temperature contours around a single symmetric electrode: a) $t = 4$ ms and b) $t = 8$ ms.

The variation of $U_{\max}$ and $\delta_{1/2}$ for the steady-state pulse-averaged velocity profile with downstream distance x is plotted logarithmically in Fig. 17, together with a best-fit line to the data. Glauert[25] predicted that for a plane laminar wall jet the velocity varies as $u \propto x^{-1/2}$ and the jet thickness varies as $\delta_{1/2} \propto x^{3/4}$. It can be seen that the best-fit exponents are in reasonable agreement to those expected from a laminar wall jet, given the lack of data in the downstream direction.

E. Temperature Profile

A similar technique has been applied with a cold-wire probe operated in constant-current mode to obtain the temperature variation around the electrode in initially static air. Here the symmetric electrode case is studied, and the plasma parameters are identical as for the results presented in Sec. III.D. The contour plot of the ensemble-averaged data after a single plasma pulse is shown in Fig. 18 at $t = 4$ and 8 ms. These show a pair of high-temperature regions moving along the wall, away from the electrode centerline with maximum temperature difference of 2.0 ± 0.1°C (compare Figs. 18a and 18b). Using the temperature as a passive tracer, these have an estimated

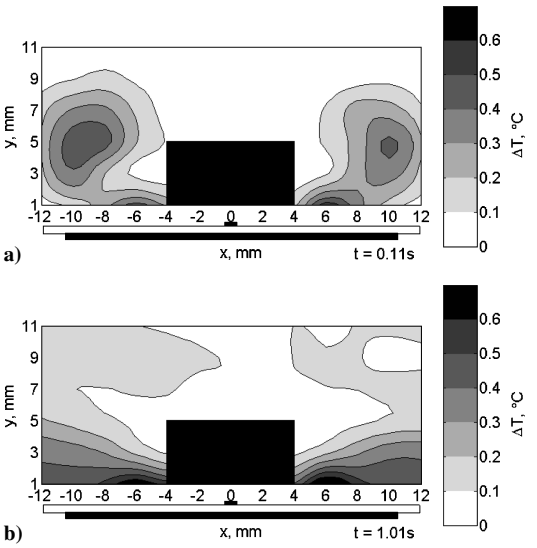

Fig. 19 Pulse-averaged temperature contours around a single symmetric electrode: a) $t = 0.11$ s and b) $t = 1.01$ s.

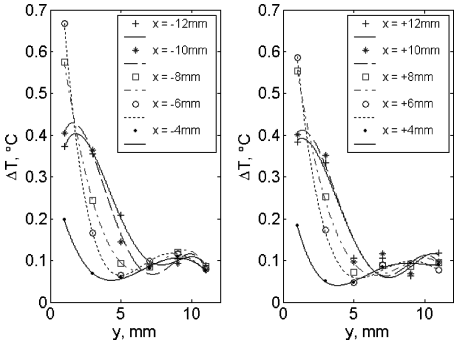

Fig. 20 Pulse-averaged temperature profiles on either side of the symmetric electrode. Curves are polynomial fits to the data points: $t = 1.01$ s.

convection velocity of 0.5 m/s. It is expected that the temperature is higher closer to the electrode. Thus there is some heat transferred to the air at the plasma-gas interface. After each individual plasma pulse, the heated air is convected laterally with the resulting wall-jet flow.

The contour plot of the temperature change, based on time-averaged data between plasma pulses, is shown at $t = 0.11$ and 1.01 s in Fig. 19. The initiation of the plasma causes two high-temperature regions to be ejected away from the electrode centerline, corresponding to the two vortex cores (Fig. 19a). These have a convection velocity of 0.1 m/s and travel at an angle of 25 deg to the wall. The maximum temperature difference is 0.5°C. After about 0.3 s, these have diffused and exited the measurement area. A steady increase in wall temperature is observed after this time, to a maximum of 0.8°C at the end of the plasma-on period. The pulse-averaged temperature profile on either side of the electrode at $t = 1.01$ s is shown in Fig. 20. Similar to the velocity data, this is nearly symmetric, as expected from the electrode geometry.

The temperature of the induced airflow is not significantly above ambient temperature. Assuming a maximum temperature difference of 50°C occurs at the plasma-air boundary (a generous approximation given the temperature profile) and a length scale of 4 mm (total length of plasma formation on both side of the electrode), the Grashof number of the configuration is $Gr = 470$. If the inertial force created by the temperature gradient were of the same order of magnitude as the buoyancy force, then $Re \sim Gr^{1/2}$. Thus, a flow of $\sim$0.1 m/s is expected. The observed flows are of greater magnitude and contrary to that expected from buoyant flow. We therefore expect that the thermal effect of the plasma is not responsible for the observed airflow.

IV. Conclusions

Two-dimensional hot-wire and cold-wire surveys have been performed around a symmetric and an asymmetric rf glow discharge plasma electrode in initially static air at atmospheric pressure. The velocity profiles show that plasma imparts momentum into the air, such that a laminar wall jet is produced emanating away from the electrode centerline. Because the plasma-induced flow is not a source of fluid, there is expected to be an entrainment region from above the electrode, whereby fluid is drawn toward the plasma to replace that ejected laterally.

The velocity profile and temperature profile show that vortices are created at the first instance of plasma formation in initially static air. These move at an angle of around 25 deg to the electrode sheet with a convection velocity of 0.1 m/s. After an initiation period of $t^* \approx 10$, the flow forms a pulsed, quasi-steady laminar wall jet.

The temperature profiles show a maximum air temperature difference of 2°C occurs at 1 mm away from the electrode sheet surface. It is unlikely that the thermal nature of the plasma is responsible for inducing the observed airflow because the temperature differences are small and the observed flow is contrary to that expected from buoyancy driven flow. The origins of the induced flowfield remain unclear. The fact that the induced flow only occurred when plasma was present does suggest that the flow is induced by some interaction between the plasma particles and the neutral gas and not just the presence of the electric field. It has been suggested that the steep electric field gradients within the plasma accelerate ions, which exchange momentum with the neutral background gas through ion-neutral collisions and thus induce a flow.[2,3,7]

The magnitude of the induced flowfield can easily be controlled by variations of the plasma excitation parameters, and the observed trends suggest that higher flow speeds could be possible. The generated flow profiles are always similar to a laminar wall jet at the low Reynolds numbers observed in these experiments. A peak velocity of 2.5 m/s has been recorded, although the true velocity will be greater at the plasma-air boundary. It is also observed that the asymmetric electrode configuration will confine the forcing in one direction and produce a jet velocity nearly double that of the symmetric actuator.

This study has been performed as a feasibility study for using the plasma actuator for flow control in the turbulent boundary layer. For successful flow control by mechanical spanwise wall oscillation, Choi et al.[20] found that a drag reduction of 45% occurred with a nondimensional wall velocity $w^+ = \Delta z \cdot \omega / 2u_\tau \approx 15$, where Δz is the amplitude of wall oscillation, $\omega\,(=2\pi f)$ is the angular velocity of wall oscillation, u_τ is the friction velocity, and f is the oscillation frequency. Choi et al.[20] used $f = 7$ Hz, $\Delta z = 70$ mm with a freestream velocity U_∞ of 2 m/s. The maximum wall velocity during the sinusoidal motion was 1.5 m/s. The flow velocities generated here are certainly capable of meeting these criteria, and it is concluded that plasma actuators will produce significant effects in low-speed test facilities.

Acknowledgments

This project is jointly funded by BAE Systems and the Engineering and Physical Sciences Research Council.

References

[1]Roth, J. R., *Industrial Plasma Engineering. Vol. 1: Principles*, Inst. of Physics Publishing, Bristol, England, U.K., 1995, Chaps. 1, 4, 11, and 12.

[2]Roth, J. R., *Industrial Plasma Engineering. Vol. 2: Applications to Nonthermal Plasma Processing*, Inst. of Physics Publishing, Bristol, England, U.K., 2001, Chaps. 15, 17, and 18.

[3]Wilkinson, S. P., "Investigation of an Oscillating Surface Plasma for Turbulent Drag Reduction," AIAA Paper 2003-1023, Jan. 2003.

[4]Johnson, G. A., and Scott, S. J., "Plasma-Aerodynamic Boundary Layer Interaction Studies," AIAA Paper 2001-3052, June 2001.

[5]Scott, S. J., Johnson, G. A., and Thornton, E., BAE Systems plc, GB Patent Application for "Turbulent Flow Drag Reduction," World Intellectual Property Organisation, International Publication WO 0/2081303, filed 26 March 2002.

[6]Scott, S. J., Johnson, G. A., and Thornton, E., BAE Systems plc, GB. Patent Application for "Turbulent Flow Drag Reduction," World Intellectual Property Organisation, International Publication WO 0/2081304, filed 26 March 2002.

[7]Roth, J. R., Sherman, D. M., and Wilkinson, S. P., "Electrohydrodynamic Flow Control with a Glow-Discharge Surface Plasma," *AIAA Journal*, Vol. 38, No. 7, 2000, pp. 1166–1172.

[8]Roth, J. R., and Sherman, D. M., "Boundary Layer Flow Control with a One Atmosphere Uniform Glow Discharge Surface Plasma," AIAA Paper 98-0328, Jan. 1998.

[9]Sherman, D. M., "Manipulating Aerodynamic Boundary Layers Using an Electrohydrodynamic Effect Generated by One Atmosphere Uniform Glow Discharge Plasma," M.S. Thesis, Univ. of Tennessee, Knoxville, TN, Aug. 1998.

[10]Corke, T. C., and Post, M. L., "Overview of Plasma Flow Control: Concepts, Optimization, and Applications," AIAA Paper 2005-0563, Jan. 2005.

[11]Corke, T. C., and Orlov, D. M., "Numerical Simulation of Aerodynamic Plasma Actuator Effects," AIAA Paper 2005-1083, Jan. 2005.

[12]Corke, T. C., Jumper, E. J., Post, M. L., and Orlov, D., "Applications of Weakly-Ionized Plasmas as Wing Flow-Control Devices," AIAA Paper 2002-0350, Jan. 2002.

[13]Post, M. L., and Corke, T. C., "Separation Control on High Angle of Attack Airfoil Using Plasma Actuators," *AIAA Journal*, Vol. 42, No. 11, 2004, pp. 2177–2184.

[14]Hultgren, L. S., and Ashpis, D. E., "Demonstration of Separation Delay with Glow-Discharge Plasma Actuators," AIAA Paper 2003-1025, Jan. 2003.

[15]Huang, J., Corke, T. C., and Thomas, F. O., "Plasma Actuators for Separation Control of Low Pressure Turbine Blades," AIAA Paper 2003-1027, Jan. 2003.

[16]Asghar, A., and Jumper, E. J., "Phase Synchronization of Vortex Shedding from Multiple Cylinder Using Plasma Actuators," AIAA Paper 2003-1028, Jan. 2003.

[17]Shyy, W., Jayaraman, B., and Andersson, A., "Modeling of Glow Discharge Induced Fluid Dynamics," *Journal of Applied Physics*, Vol. 92, No. 11, 2002, pp. 6434–6443.

[18]Enloe, C. L., McLaughlin, T. E., VanDyken, R. D., Kachner, K. D., Jumper, E. J., Corke, T. C., Post, M., and Haddad, O., "Mechanisms and Responses of a Single Dielectric Barrier Plasma Actuator: Geometric Effects," *AIAA Journal*, Vol. 42, No. 3, 2004, pp. 595–604.

[19]Enloe, C. L., McLaughlin, T. E., VanDyken, R. D., Kachner, K. D., Jumper, E. J., Corke, T. C., "Mechanisms and Responses of a Single Dielectric Barrier Plasma Actuator: Plasma Morphology," *AIAA Journal*, Vol. 42, No. 3, 2004, pp. 595–604; also AIAA Paper 2003-1021, Jan. 2003.

[20]Choi, K.-S., DeBisschop, J.-R., and Clayton, B. R., "Turbulent Boundary-Layer Control by Means of Spanwise-Wall Oscillation," *AIAA Journal*, Vol. 36, No. 7, 1998, pp. 1157–1163.

[21]Liu, S., and Neiger, M., "Excitation of Dielectric Barrier Discharges by Unipolar Submicrosecond Square Pulses," *Journal of Physics D: Applied Physics*, Vol. 34, No. 11, 2001, pp. 1632–1638.

[22]Gibalov, V., and Pietsch, G., "The Development of Dielectric Barrier Discharges in Gas Gaps and on Surfaces," *Journal of Physics D: Applied. Physics*, Vol. 33, 2000, pp. 2618–2636.

[23]Willis, J. A. B., "The Correction of Hot-Wire Readings for Proximity to a Solid Wall," *Journal of Fluid Mechanics*, Vol. 12, 1962, pp. 388–396.

[24]Hutchins, N., and Choi, K.-S., "Accurate Measurements of Local Skin Friction Coefficient Using Hot-Wire Anemometry," *Progress in Aerospace Sciences*, Vol. 38, No. 4, 2002, pp. 421–446.

[25]Glauert, M. B., "The Wall Jet," *Journal of Fluid Mechanics*, Vol. 1, 1956, pp. 625–643.

[26]Roth, J. R., Madhan, R. C. M., Yadav M., Rahel, J., and Wilkinson, S. P., "Flow Field Measurements of Paraelectric, Peristaltic, and Combined Plasma Actuators Based on the One Atmosphere Uniform Glow Discharge Plasma (OAUGDP)," AIAA Paper 2004-845, Jan. 2004.

[27]Chun, D. H., and Schwarz, W. H., "Stability of the Plane Incompressible Viscous Wall Jet Subjected to Small Disturbances," *Physics of Fluids*, Vol. 10, No. 5, 1967, pp. 911–915.

M. Auweter-Kurtz
Associate Editor